The Astrophysical Journal, 920:97 (11pp), 2021 October 20 https://doi.org/10.3847/1538-4357/ac185e

The Nuclear Star Cluster and Nuclear Stellar Disk of the Milky Way: Different Stellar Populations and Star Formation Histories

Francisco Nogueras-Lara[1], Rainer Schödel[2], and Nadine Neumayer[1]
[1] Max-Planck Institute for Astronomy, Königstuhl 17, D-69117 Heidelberg, Germany; nogueras@mpia.de
[2] Instituto de Astrofísica de Andalucía (CSIC), Glorieta de la Astronomía s/n, E-18008 Granada, Spain
Received 2021 June 21; revised 2021 July 15; accepted 2021 July 26; published 2021 October 20

Abstract

The Milky Way's nuclear stellar disk (NSD) and nuclear star cluster (NSC) are the main features of the Galactic center. Nevertheless, their observation is hampered by the extreme source crowding and high extinction. Hence, their relation and formation scenario are not fully clear yet. We aim to detect the stellar populations from the NSC and the NSD along the line of sight toward the NSC and assess whether they have different stellar populations and star formation histories. We analyzed the color–magnitude diagram, K_s versus $H-K_s$, of a region of $8\farcm2 \times 2\farcm8$ centered on the NSC, and detected two different stellar groups with different extinctions. We studied their red clumps to find the features associated with each of the stellar populations. We obtained that the two groups of stars correspond to the NSD and the NSC and found that they have significantly different stellar populations and star formation histories. We detected a double red clump for the NSD population, in agreement with previous work, whereas the NSC presents a more complex structure well fitted by three Gaussian features. We created extinction maps to analyze the extinction variation between the detected stellar groups. We found that the high-extinction layer varies on smaller scales (arcseconds) and that there is a difference of $A_{K_s} \sim 0.6$ mag between both extinction layers. Finally, we obtained that the distance toward each of the stellar populations is compatible with the Galactic center distance and found some evidence of a slightly closer distance for the NSD stars ($\sim 360 \pm 200$ pc).

Unified Astronomy Thesaurus concepts: Galactic center (565); Galaxy structure (622); Red giant clump (1370); Interstellar dust extinction (837)

1. Introduction

The center of the Milky Way is the closest galactic nucleus located only ∼8 kpc from Earth (e.g., Gravity Collaboration et al. 2018; Do et al. 2019). It allows us to resolve individual stars down to milliparsec scales and analyze in great detail its structure and stellar population (e.g., Genzel et al. 2010; Schödel et al. 2014). Therefore, it is a perfect laboratory to study galactic nuclei and their role in a wider context of galaxy evolution.

The Galactic center (GC) hosts two main structures: (1) the nuclear stellar disk (NSD), a disk-like structure with a mass of $\sim 7 \times 10^8\, M_\odot$ and radius of ∼200 pc (e.g., Launhardt et al. 2002; Nishiyama et al. 2013; Gallego-Cano et al. 2020; Sormani et al. 2020), that partially overlaps with the dense clouds of gas of the central molecular zone (e.g., Morris & Serabyn 1996); and (2) the nuclear star cluster (NSC), a massive stellar cluster ($\sim 2.5 \times 10^7\, M_\odot$, e.g., Launhardt et al. 2002; Schödel et al. 2014; Feldmeier-Krause et al. 2017; Do et al. 2019; Sormani et al. 2020) centered on the supermassive black hole Sagittarius A*, with an effective radius of ∼5 pc (e.g., Graham & Spitler 2009; Schödel 2011; Feldmeier-Krause et al. 2017; Gallego-Cano et al. 2020).

In spite of its proximity, the observation of the GC is hampered by the extreme source crowding and the high interstellar extinction that limits its analysis to the infrared regime (e.g., Nishiyama et al. 2008; Schödel et al. 2010; Nogueras-Lara et al. 2018a, 2020a). In this way, the relation between the NSC and the NSD, and their formation processes are not well understood yet (e.g., Launhardt et al. 2002; Nogueras-Lara et al. 2020b; Schödel et al. 2020). There is some evidence that the NSC and the NSD host different stellar populations with different star formation histories (SFHs, e.g., Nogueras-Lara et al. 2020b; Schödel et al. 2020; Schultheis et al. 2021). Both components seem to have a predominantly old stellar population ($\gtrsim$8 Gyr), followed by several billion years of quiescence. Nevertheless, the NSC seems to host a ∼3 Gyr-year-old intermediate-age population in the NSC, which cannot be found in the NSD. On the other hand, there is evidence of an important ∼1 Gyr star formation event associated with the NSD, which is not found when analyzing the stellar population from the NSC (Nogueras-Lara et al. 2020b; Schödel et al. 2020).

In this paper, we aim to assess whether the stellar populations of the NSC and the NSD are actually different. For this, we analyze the red clump (RC) features (e.g., Girardi 2016) of a region centered on the NSC. We use photometric data in the H and K_s bands and clearly detect two stellar groups with different extinctions that correspond to the NSC and the NSD. We find that the stellar populations belonging to each of the extinction groups are significantly different and explain the differences with different formation histories.

2. Data

2.1. HAWK-I Data

We used H and K_s photometry obtained with the NIR camera High Acuity Wide Field K-band Imager (HAWK-I; Kissler-Patig et al. 2008), placed at the ESO Very Large Telescope in Chile. The observations were taken in 2013 and constituted a pilot study for the GALACTICNUCLEUS (GNS) survey (a high-angular-resolution photometric survey of the GC; Nogueras-Lara et al. 2018a, 2019b) and were presented and described in Nogueras-Lara et al. (2018a). We used these data because the observing conditions were better than for the analogous region in the GNS

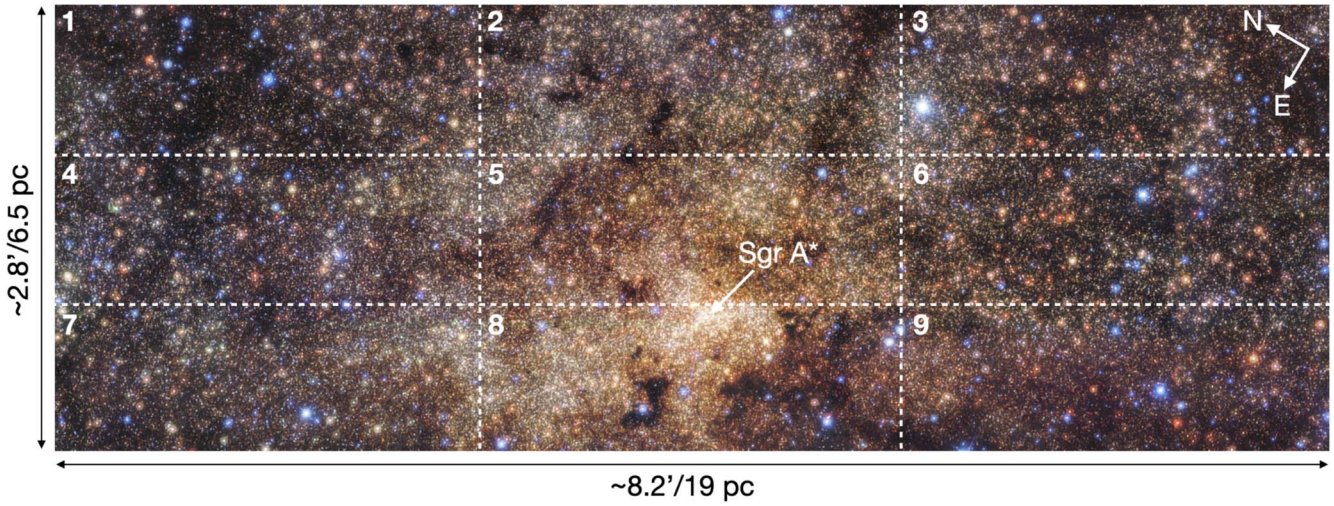

Figure 1. GALACTICNUCLEUS false-color image (using J, H, and K_s as blue, green, and red, respectively) of the analyzed region. The white arrow indicates the position of the supermassive black hole (Sgr A*) at the center of the Galaxy. The white dashed lines indicate the subregions used for the analysis shown in Section 6.

survey (see Table 1 in Nogueras-Lara et al. 2018a). The best conditions are crucial in this most crowded field of the Galaxy and imply that the H and K_s photometry of the 2013 data is around 1 mag deeper than in the GNS survey.

The observations consist of four independent fixed pointings designed to cover the cross-shaped gap between the four HAWK-I detectors. The observed region was centered on the coordinates ($17^h45^m37\overset{s}{.}70$, $-29°00'05\overset{''}{.}70$) covering a total size of $8\overset{'}{.}2 \times 2\overset{'}{.}8$ ($\sim$19 pc $\times$ 6.5 pc), as shown in Figure 1. Each of the pointings included 512 frames with a detector integration time (DIT) of 0.83 s (for further details, see Section 2 in Nogueras-Lara et al. 2018a). We processed them following a standard reduction (dark, bias, flat-fielding) and dedicated sky subtraction to later apply the speckle holography algorithm optimized for crowded fields, as explained in Schödel et al. (2013). The detectors were treated independently throughout the process. We obtained point-spread function photometry for each of them using the Starfinder algorithm (Diolaiti et al. 2000). We created the final catalog merging all the detectors, as explained in Nogueras-Lara et al. (2018a). We reached 5σ detections at $H \sim 21$ mag and $K_s \sim 20$ mag. The uncertainties were below 0.05 mag at $H \sim 18$ mag and $K_s \sim 17$ mag. The zero point was calibrated using the SIRIUS/IRSF survey (e.g., Nagayama et al. 2003; Nishiyama et al. 2006) and its systematic uncertainty was $\sim$0.04 mag (Nogueras-Lara et al. 2018a).

We also used H and K_s data from the GNS survey to analyze a control region to test the obtained results. The survey used a slightly different setup in comparison to the pilot study (for further details, see Nogueras-Lara et al. 2018a, 2019b). Both GNS and the pilot study reached $\sim 0\overset{''}{.}2$ angular resolution in the JHK_s bands.

3. Color–Magnitude Diagram

Figure 2 shows the K_s versus $H - K_s$ color–magnitude diagram (CMD) of the target region. Given the extreme extinction along the line of sight toward the GC, a simple color cut of $H - K_s > 1.35$ mag allowed us to effectively remove the foreground population belonging to the Galactic disk and to the inner Galactic bulge (e.g., Nogueras-Lara et al. 2018b, 2019b; Sormani et al. 2020; Schultheis et al. 2021; Nogueras-Lara et al. 2021a). Possible remaining contamination from the inner bulge accounts for less than 25% of the stars beyond that color cut, according to the analysis carried out by Schultheis et al. (2021) for a similar color cut and line of sight (see their Section 3.1).

3.1. Different Stellar Groups

We visually identified two different stellar groups, which correspond to a low- and high-extinguished stellar population around $H - K_s \sim 1.5$ mag and $H - K_s \sim 2$ mag, respectively. They appear as clearly distinct populations in an HST/WFC3 CMD F153M versus F105W − F153M for the innermost $2' \times 2'$, as shown in Figure 16 in Nogueras-Lara et al. (2018a).

To study the detected stellar populations, we defined two regions in the CMD covering the RC features of each of the stellar populations, as indicated in Figure 2. We selected similar vertical sizes of the selection boxes associated with each of the stellar populations in order to easily compare them in the subsequent analysis. Given that both stellar populations are separated due to the differential extinction, we avoided the stars around $H - K_s \sim 1.7$ mag when defining the regions to be analyzed. This is because that region corresponds to a transition region where stars from both stellar populations might appear, complicating the independent analysis.

We also limited the selection of the faint end of the RC features due to the completeness of the data. Given the extremely high number of stars in the analyzed region, the incompleteness is dominated by the source crowding (so the sensitivity is not significantly affecting the completeness in these crowded regions). In this way, we obtained the completeness solution using the technique described by Eisenhauer et al. (1998) and previously applied to similar data sets as the GNS survey (see Section 3.1.2 in Nogueras-Lara et al. 2020a). It computes the critical distance at which a star of a given magnitude can be detected near a brighter star and uses this parameter to estimate the completeness for the real sources in the data set. We applied this method to compute the two-thirds completeness of the data, dividing the observed region into nine smaller subregions (see Figure 1). The final completeness solution was obtained by averaging over the results for each of the defined subregions. The reference stars were selected restricting the selection boxes in agreement with the obtained completeness (colored boxes in Figure 2).

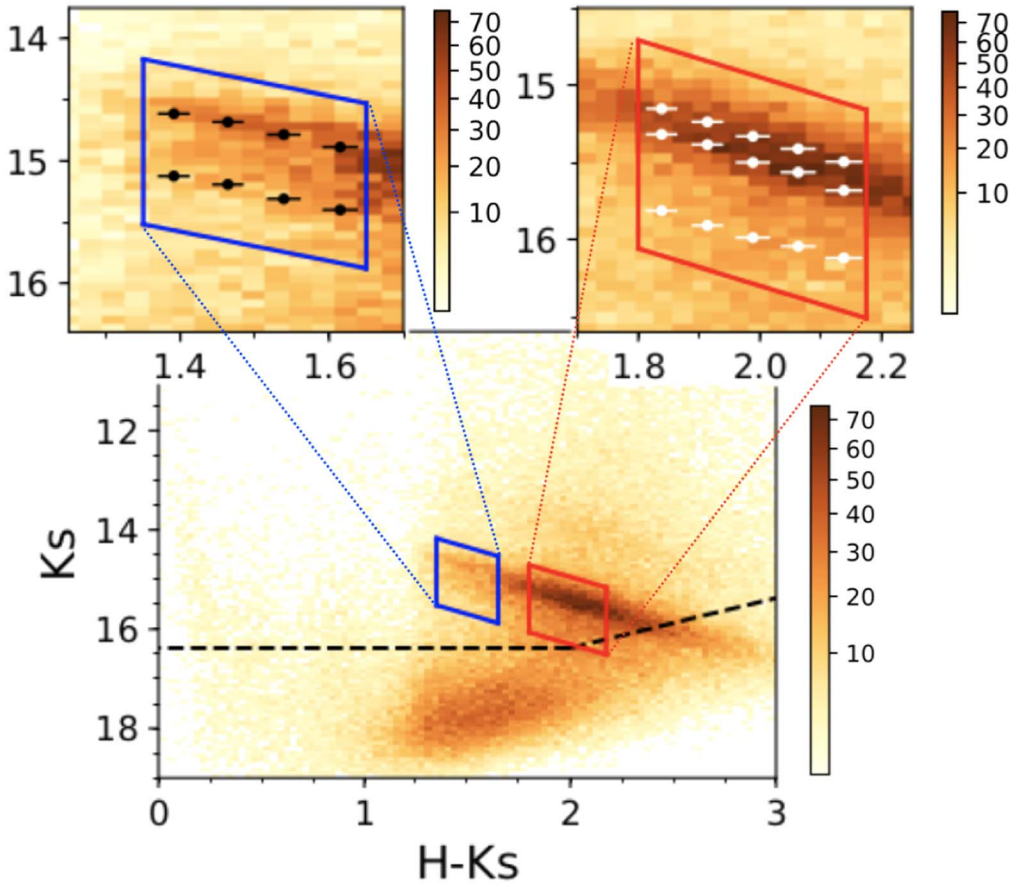

Figure 2. Color–magnitude diagram K_s vs. $H - K_s$ corresponding to the target region. The color code corresponds to stellar densities using a power stretch scale. The black dashed line indicates the two-thirds completeness level of the data. The blue and red parallelograms show the reference stars that we consider in Section 3.1 for the low- and high-extinction groups. The zoom-in panels depict the best fit found in the RC region using a GMM analysis as specified in Figure 3.

We used the SCIKIT-LEARN Python function GaussianMixture (GMM; Pedregosa et al. 2011) to independently analyze each of the different extinction groups. We divided the selected CMD regions along the x-axis ($H - K_s$ color) into sections of 0.075 mag width and used the Bayesian information criterion (BIC; Schwarz 1978) and the Akaike information criterion (AIC; Akaike 1974) to compare three different models considering one, two, and three Gaussian distributions to fit the data within each bin. Figure 3 shows the best fits obtained for each of the vertical bins. In all cases, we detected a two-Gaussian distribution for the low-extinguished stellar population, whereas the high-extinguished one presented a three-Gaussian distribution. Figure 2 depicts the obtained results in the zoom-in panel, where the obtained features follow the reddening vector. In particular, we computed the slopes of each of the detected features and obtained $s_{\text{low bright}} = 1.24 \pm 0.13 \pm 0.12$, $s_{\text{low faint}} = 1.29 \pm 0.10 \pm 0.08$, $s_{\text{high bright}} = 1.16 \pm 0.01 \pm 0.03$, $s_{\text{high intermediate}} = 1.21 \pm 0.09 \pm 0.02$, and $s_{\text{high faint}} = 1.01 \pm 0.06 \pm 0.10$, where the subscripts "low" and "high" indicate the corresponding extinction group. The uncertainties refer to the statistical and the systematic ones, respectively. The statistical uncertainty was computed using a jackknife resampling method, systematically leaving out one of the data points to calculate the slope (e.g., Nogueras-Lara et al. 2020a, 2021c). The systematics were estimated varying the selection boxes and the size and number of vertical bins. The obtained slopes are consistent within the uncertainties with the slope, $s = 1.19 \pm 0.04$, of the extinction curve derived in Nogueras-Lara et al. (2019a, 2020a) using the GNS catalog.

3.2. Comparison with a Control Region

We repeated the analysis using a control region of the same size that is located at a distance to the center of the NSC of more than six effective NSC radii (see Figure 4, e.g., Schödel et al. 2014; Feldmeier-Krause et al. 2017; Gallego-Cano et al. 2020).

We built a K_s versus $H - K_s$ CMD (Figure 5) and computed the two-thirds completeness due to crowding using the previously explained technique and the results for the GNS survey in Nogueras-Lara et al. (2020a). We obtained better data completeness in comparison to the target region because the control region does not contain the NSC, and the crowding is thus less important.

The RC in the control field appears as a continuous feature, without any visible change as a function of extinction. We proceeded in our analysis of the RC region of the CMD exactly as described previously. Figure 5 shows the results. At both high and low extinction, we find the same feature in the RC region of the CMD of the control field. In fact, the high-extinction features in the control field can be simply obtained by additional reddening of the low-extinction features. This is markedly different from the target field, where the high-extinction CMD region shows an additional feature associated with the RC. The difference between the target and control regions is the presence of the NSC in the former. The NSC stars occupy the high-extinction part in the target region CMD.

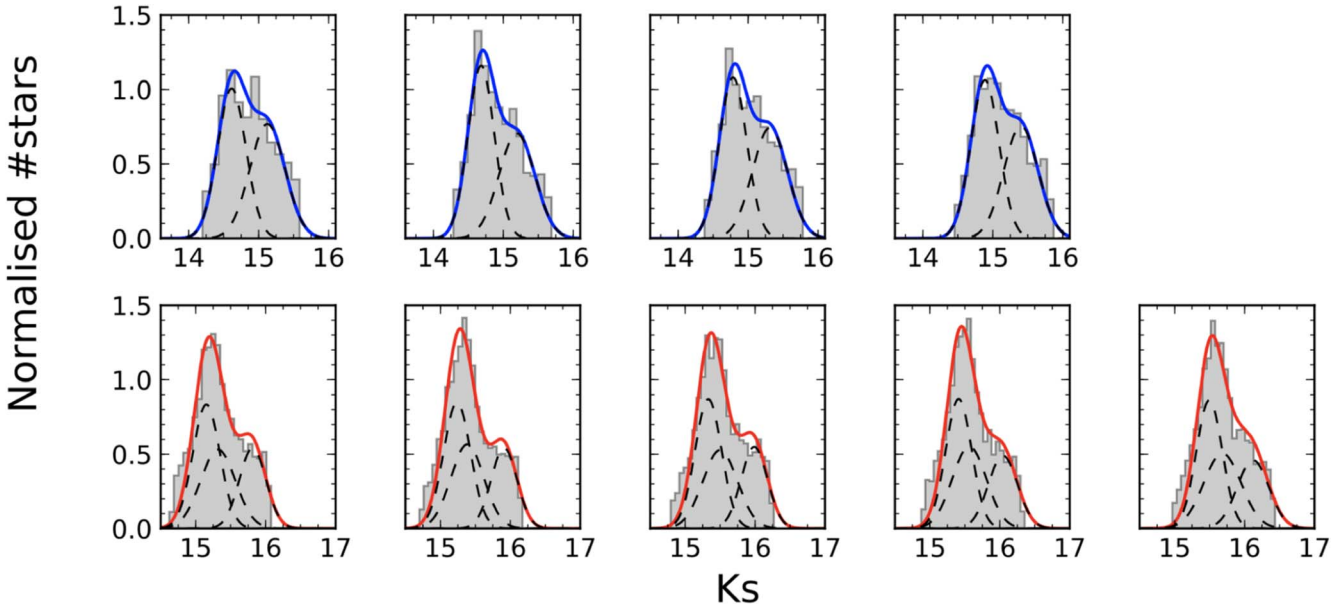

Figure 3. Best-fit models obtained for each of the vertical cuts through the CMD defined in Section 3.1, to analyze the RC features in the K_s vs. $H - K_s$ CMD. The gray histograms show the K_s distribution of each of the vertical cuts. The blue and the red solid lines depict the models corresponding to the best fits for the low- and the high-extinguished stellar populations, respectively. The black dashed lines indicate the Gaussian models used for the fits. Upper panels: from left to right, each of the four bins of 0.075 mag starting from $H - K_s = 1.35$ mag corresponding to the low-extinguished stellar population. Lower panels: from left to right, each of the five sections of 0.075 mag starting from $H - K_s = 1.8$ mag corresponding to the high-extinguished stellar population.

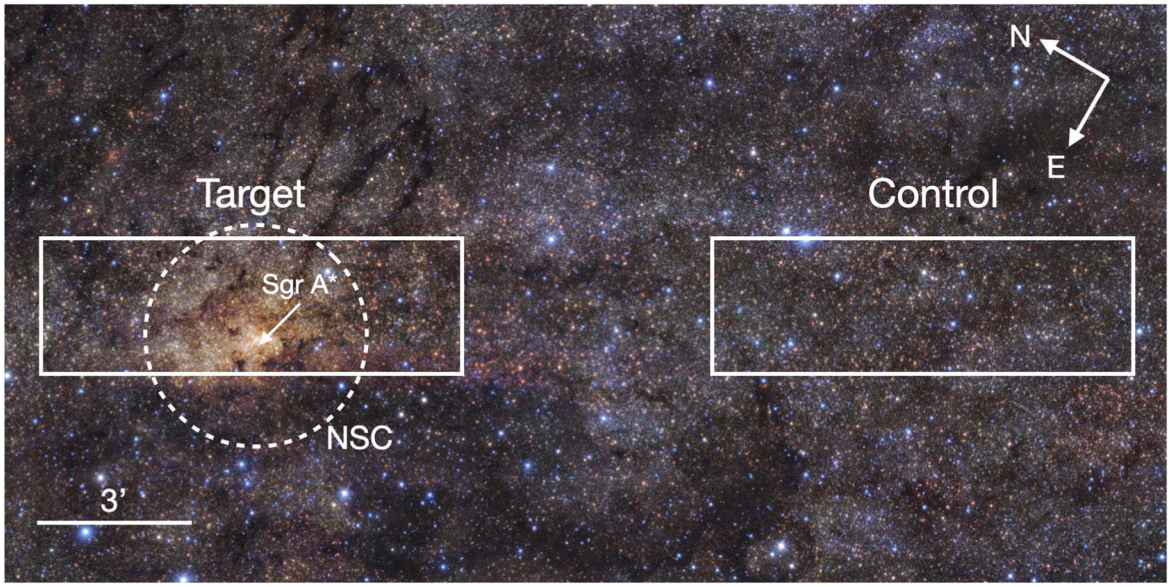

Figure 4. Scheme of the target and control regions selected. The background image corresponds to a false-color image (JHK_s) from the GNS survey. The white dashed circle indicates the effective radius of the NSC. The position of Sgr A* is indicated as a reference.

3.3. Discussion

The presence of several RC features can be explained by two different scenarios: (a) stellar populations at different distances and (b) RC stars with different ages and/or metallicities (e.g., Ferraro et al. 2009; Girardi 2016). To further analyze this, we computed the K_s distance between the detected features in the target region. We obtained

(1) $\Delta K_{s\,\mathrm{low}} = 0.52 \pm 0.01 \pm 0.02$ mag, where the subscript "low" refers to the low-extinguished stellar population; (2) $\Delta K_{s\,\mathrm{high\ 1}} = 0.16 \pm 0.01 \pm 0.01$ mag, where the subscripts "high" and "1" indicate the difference in magnitude between the brightest and the secondary feature of the high-extinguished stellar population; and (3) $\Delta K_{s\,\mathrm{high\ 2}} = 0.65 \pm 0.02 \pm 0.05$ mag, where the subscript "2" refers to the K_s magnitude distance between the brightest and the faintest features in the high-extinguished stellar population. The ΔK_s values were obtained averaging over the magnitude differences of the points shown in Figure 2. The first uncertainty corresponds to the statistical one and was estimated via the standard deviation of the measurements. The second one refers to the systematic uncertainty and was computed repeating the analysis varying the limits of the selection box and using different bin-width sizes.

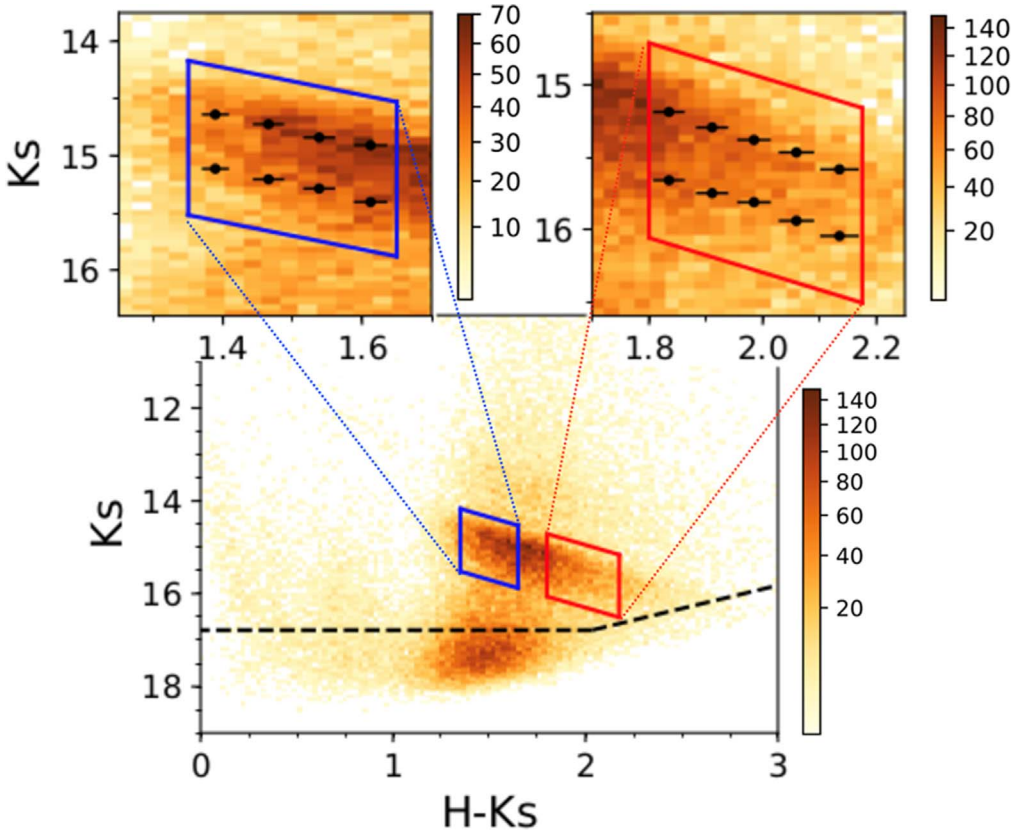

Figure 5. Color–magnitude diagram K_s vs. $H - K_s$ corresponding to the control region. The color code corresponds to stellar densities using a power stretch scale. The black dashed line indicates the two-thirds completeness level of the data. The blue and red parallelograms show the reference stars that we consider in Section 3.1 for the low- and high-extinction groups. The zoom-in panels depict the best fit found in the RC region using a GMM analysis.

Given the high crowding and extreme extinction in the GC (e.g., Nishiyama et al. 2008; Schödel et al. 2010; Nogueras-Lara et al. 2018a, 2020a), scenario (a) (having stellar populations at different distances) is quite unlikely and would be only possible for small distances between the stellar populations. Nevertheless, even for the magnitude difference between the brightest and the secondary RC features measured for the high-extinguished stellar group ($\Delta K_{s\,\mathrm{high\,1}} = 0.16 \pm 0.01 \pm 0.01$ mag), this distance difference would be ∼600 pc beyond the GC, at the GC distance of ∼8 kpc (e.g., Gravity Collaboration et al. 2018; Do et al. 2019). This would imply that there is a stellar substructure as dense as the NSC located behind the GC, which is highly improbable. The situation becomes even more extreme for the stellar populations associated with larger magnitude differences. Moreover, due to the extreme extinction, stellar populations located at significantly different distances should show some difference in reddening, implying a shift toward redder colors in the $H - K_s$ axis in the CMD with respect to closer components. This was not found for the RC components measured within each of the extinction groups. Thus, we can safely exclude this scenario. Hence, the more likely explanation for the different number of features between the low- and the high-extinguished groups of stars is a difference in their RC stellar population.

The two-Gaussian distribution found for the low-extinguished group of stars is in agreement with the stellar population obtained for the NSD, where previous work found a double-RC feature with a magnitude difference of $\Delta K_s \sim 0.5$ mag (e.g., Rui et al. 2019; Nogueras-Lara et al. 2020b, 2021c). This is also in agreement with the analysis of the control region, where we did not observe any difference between the two selection boxes analyzed in the RC. We obtained a $\Delta K_{s\,\mathrm{low}} = 0.47 \pm 0.02 \pm 0.02$ mag for the first selection box that corresponds to the low-extinguished stellar group in the target region, and $\Delta K_{s\,\mathrm{high}} = 0.46 \pm 0.02 \pm 0.05$ mag for the selection box corresponding to the high-extinguished stellar group in the target region. The uncertainties were obtained as previously explained for the target region.

Therefore, we conclude that the low-extinguished stellar group corresponds to the NSD, as it is seen in front of the NSC due to the different extinctions. On the other hand, we believe that the three-Gaussians distribution is associated with the more complex stellar population from the NSC. This is in agreement with previous studies that suggest that the SFH of the NSC might be different from that of the NSD (e.g., Schödel et al. 2020; Schultheis et al. 2021). In particular, according to the SFH derived in Schödel et al. (2020), the bulk of the stars is old (80% of the stellar mass older than 10 Gyr), followed by a quiescent period that ended around 3 Gyr ago with the formation of ∼15% of the stellar mass. Finally, a few percent of the stars were formed in the past few 100 Myr. In this way, the three Gaussian features that we detect in our analysis agree with the fit of theoretical K_s luminosity functions in Figure 10 of Schödel et al. (2020), where the two brightest peaks would be produced by the old and intermediate-age stellar populations, and the third one would be the consequence of the formation of the red giant branch bump (RGBB; e.g., Nataf et al. 2011; Wegg & Gerhard 2013). The RGBB is also present in the NSD stellar population but partially overlaps with the RC feature from the ∼1 Gyr stellar population, producing a closer secondary peak (see Section 3.4.1).

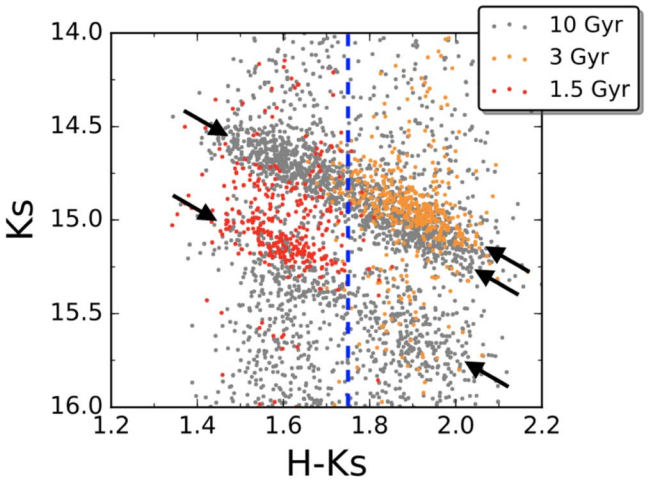

Figure 6. Synthetic K_s vs. $H - K_s$ CMD using PARSEC models to simulate the RC distribution found according to the different stellar populations from the NSD and the NSC. The blue dashed line indicates the rough separation between both components due to reddening. The black arrows show the different RC features detected in our analysis.

3.4. Synthetic Models

3.4.1. CMD Simulation

To assess our previous conclusions, we built a simple synthetic K_s versus $H - K_s$ CMD to simulate the main stellar populations in the NSD and the NSC, using PARSEC models (release v1.2S + COLIBRI S_37, Bressan et al. 2012; Chen et al. 2014, 2015; Tang et al. 2014; Marigo et al. 2017; Pastorelli et al. 2019, 2020). Because our purpose is just to detect the main features in the RC region of the CMD, we simply assumed approximately similar masses for the stellar populations belonging to the NSD and the NSC. We only used the stellar models that significantly account for the stars in the RC feature following the results obtained by Nogueras-Lara et al. (2020b) and Schödel et al. (2020). Namely, for the NSD, we chose an old stellar model of 10 Gyr (∼95% of the total stellar mass) and a younger one of 1.5 Gyr (∼5% of the total stellar mass). We simulated the NSC using the same old stellar population (10 Gyr), and an intermediate-age one of 3 Gyr (accounting for ∼20% of the total stellar mass). We selected metal-rich models (around twice solar metallicity) for all the models, in agreement with previous work (e.g., Feldmeier-Krause et al. 2017; Schultheis et al. 2019, 2021). To simulate the extinction, we used the extinction curve in Nogueras-Lara et al. (2020a), and the values obtained in Table 3 of Nogueras-Lara et al. (2018a) for the reddening of each of the extinction groups. We applied the extinction randomly assigning extinction values to each star from a Gaussian distribution centered on the mean extinction value for each of the extinction groups. The standard deviation of the Gaussian distributions was $dA_{K_s} \sim 0.1$ mag, in agreement with the extinction distributions in Nogueras-Lara et al. (2018a). We randomly generated the photometric uncertainties assuming a Gaussian distribution for each of the stars with a standard deviation of 0.025 mag, which corresponds to the expected mean uncertainty for the data used at the RC magnitude for H and K_s. Figure 6 shows the obtained result. The black arrows in the figure depict the obtained overdensities that are in agreement with the features obtained in the analysis of the target region and discussed in the previous section.

3.4.2. Simulation of K_s Luminosity Functions

We also built synthetic K_s luminosity functions (KLFs) for each of the stellar populations to compare them with the results obtained in Section 3.3. We used the corresponding theoretical models, assuming the previously explained uncertainties. To simulate the scatter associated with a real dereddened KLF (e.g., Section 6 in Nogueras-Lara et al. 2021b), we varied the magnitude of each star assuming a Gaussian distribution centered on its real magnitude with a standard deviation of 0.1 mag. Figure 7 shows the obtained KLFs for each of the stellar populations. We stress that this is a simple model that aims to check our results considering only the stellar populations that significantly contribute to the RC features, assuming that all stars are at the same distance. Therefore, the RC features are more prominent in comparison with real data.

We computed the distance between the Gaussian features, the relative fraction of stars belonging to each RC feature, and their associated uncertainties, resorting to 100 Monte Carlo (MC) simulations. For each of them, we produced the KLF generating the corresponding magnitude uncertainties and the scatter associated with the dereddening process, as previously explained. We fitted the RC features of each KLF using a two-Gaussian model for both cases, the NSD and the NSC. For the NSC, we assumed a single Gaussian to account for the bright RC for simplicity. We obtained mean magnitude differences of $dK_{s0\,\mathrm{NSD}} = 0.51 \pm 0.05$ mag and $dK_{s0\,\mathrm{NSC}} = 0.66 \pm 0.03$ mag, with the distance in magnitude larger for the NSC stellar population, as obtained in Section 3.3. The uncertainties correspond to the standard deviation of the results obtained for each MC sample. Computing the ratio between the number of stars in each Gaussian feature, we obtained average values of $\mathrm{ratio_{NSD}} = 1.25 \pm 0.28$ and $\mathrm{ratio_{NSC}} = 2.72 \pm 0.29$, where the uncertainties were estimated using the standard deviation of the distributions. We computed mean experimental values from the Gaussian fits in Figure 3 averaging over the values obtained for each vertical cut (and combining the bright features for the high-extinguished stellar population). We obtained $\mathrm{ratio_{low}} = 1.14 \pm 0.06$ and $\mathrm{ratio_{high}} = 2.87 \pm 0.05$, where the uncertainties correspond to the standard deviation of the measurements. Our results show that the relative fraction of stars between the features is different for each extinction group and that it is compatible with the expected stellar population from the NSD and the NSC. Nevertheless, the computed ratios do not correspond with the real stellar ratios between the RC from different ages and/or the RGBB. This would require a more in-depth analysis taking into account the exponential background associated with the KLF (for further details see e.g., Wegg & Gerhard 2013; Nogueras-Lara et al. 2018b).

4. Extinction Maps

The detection of the low- and the high-extinguished stellar groups associated with the NSD and the NSC, respectively, is possible given the different extinctions associated with each of the stellar populations. In this way, we also produced extinction maps to compute the extinction variations.

To create the extinction maps associated with each group of stars, we used the method described in Nogueras-Lara et al. (2018a, 2018b, 2020b). Namely, we used RC and red giant stars fulfilling $K_s \in [13.75, 15.75]$ mag and $H - K_s \in [1.35, 1.65]$ mag for the NSD stellar population and $K_s \in [14.5, 16.75]$ mag and $H - K_s \in [1.8, 2.175]$ mag for the NSC. We

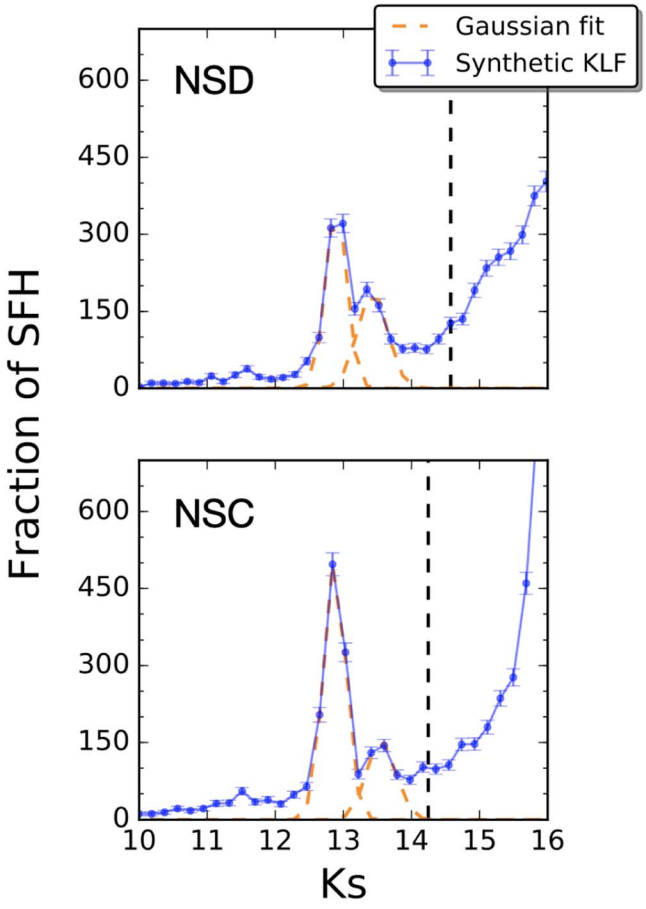

Figure 7. Synthetic dereddened K_s luminosity functions for the NSD (upper panel) and the NSC (lower panel) corresponding to one of the MC realizations. The black dashed lines indicate the two-thirds completeness limit due to crowding considering dereddened photometry. The orange dashed lines indicate Gaussian fits to the RC features.

defined a pixel size of 3″ and computed the associated extinction to each pixel using the five closest reference stars (within a maximum radius of 7.″5). We computed the extinction using the equation

$$A_{K_s} = \frac{K_s - H - (K_s - H)_0}{(A_{K_s}/A_H) - 1}, \quad (1)$$

where A_{K_s} is the extinction in the K_s band, H and K_s are the photometric measurements, the subscript 0 indicates the intrinsic color, and A_{K_s}/A_H is the used extinction curve and equals 1.84 ± 0.03 (Nogueras-Lara et al. 2019a, 2020a). To take into account the different distances of the stars to a given extinction map pixel, we used an inverse distance weight method, as explained in Section 7 in Nogueras-Lara et al. (2018a).

We also built uncertainty maps using a jackknife resampling method, computing the extinction variation systematically excluding one of the stars used for the extinction calculation associated with each pixel (see Section 7 in Nogueras-Lara et al. 2018a). The systematic uncertainties were estimated varying the quantities involved in Equation (1) within their associated uncertainties.

Figure 8 shows the obtained extinction maps and their associated uncertainties. The mean extinction values are $A_{K_s\,\mathrm{NSD}} = 1.70 \pm 0.07$ mag and $A_{K_s\,\mathrm{NSC}} = 2.27 \pm 0.09$ mag. The uncertainties refer to the standard deviation of the value for each map. The mean statistical uncertainty obtained from the uncertainty maps is ∼2%, and the systematic uncertainty is ∼5%.

The obtained average extinctions are significantly different and point toward two different layers. We also observed that the variation of the extinction across the field associated with the NSC seems to happen on shorter spatial scales in comparison with the extinction map obtained for the NSD (see Figure 8). This is in agreement with the previous work by Nogueras-Lara et al. (2018a) using an independent data set (the central pointing of the GNS survey; Nogueras-Lara et al. 2019b). Therefore, the extinction maps are consistent with having a first extinction layer associated with the interstellar medium in front of the GC (the first extinction map, upper panels in Figure 8) and a secondary layer corresponding to extinction inside the NSD and the CMZ, that varies on shorter spatial scales (arcseconds), corresponding to the secondary layer (bottom maps in Figure 8)). In this way, the low-extinguished stellar group agrees well with the stellar population from the NSD and the high-extinguished one corresponds to the stellar population from the NSC.

5. NSD Contamination of the NSD Region in the CMD

The strong variation of the extinction makes it possible to identify the NSD and the NSC using the K_s versus $H - K_s$ CMD. Nevertheless, there is some correlation between the extinction layers corresponding to each component as shown in Figure 8. Therefore, some pollution from the NSD in the NSC feature is expected. To estimate this contamination, we divided the target regions for each of the extinction groups analyzed in Figure 2 into small vertical cuts of 0.05 mag and computed the number of stars belonging to each of them. Averaging over the results for each of the groups, we obtained the mean number of stars for each component. Assuming that the density of the NSD stars is approximately constant for the covered extinction range, we can estimate an upper limit to the stars from the NSD present in the NSC sample, computing the ratio between the mean number of stars of each component. We obtained that up to ∼30% of the stars in the NSC feature might belong to the NSD.

We also tested the influence of completeness on this result. We used the technique presented in Section 3.1.2 in Nogueras-Lara et al. (2020a). We selected a completeness reference level (60%) in the CMD and randomly removed stars in the CMD, in agreement with the completeness solution, to normalize them with respect to the reference level. We created 100 MC samples using this technique and estimated the possible contamination from the NSD on the NSC for each of them, as previously explained. We did not observe any significant difference with respect to the previous result.

6. The Stellar Population across Different Lines of Sight

We also analyze the distribution of both extinction groups (corresponding to the NSD and the NSC), in the CMD across different lines of sight. For this, we divided the observed field into nine equally sized regions, as shown in Figure 1. Figure 9 shows the CMDs associated with each of the regions, where the completeness due to crowding is computed for each of them, following the method explained in Section 3.1. We found that the two detected stellar populations appear even more clearly separated for the majority of the regions. This separation correlates well with the difference in extinction between the extinction groups. In this way, we calculated the extinction

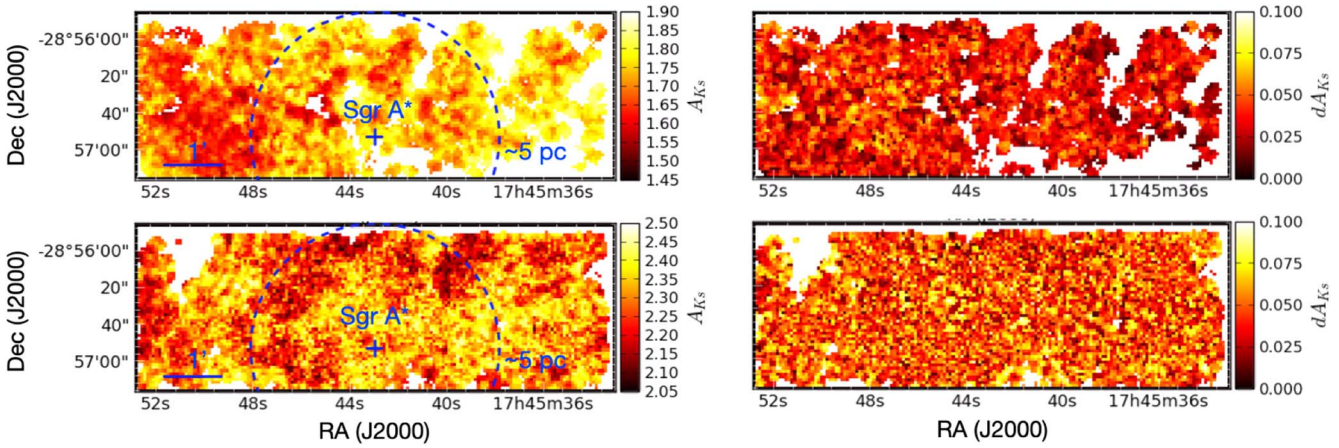

Figure 8. Left column: extinction maps obtained for the low-extinguished group of stars (upper panel), and the high-extinguished one (lower panel). The color scale is linear and has different limits for each extinction map according to its dynamical range. The blue dashed line indicates the effective radius of the NSC (e.g., Gallego-Cano et al. 2020). The position of Sgr A* is also indicated. Right column: associated uncertainty maps computed as indicated in Section 4. The color scales are the same for both uncertainty maps. White pixels in the maps indicate that the number of reference stars was not enough to compute an associated extinction value.

difference between groups for the different regions using the extinction maps previously computed (see Section 4). We obtained that the difference is $\Delta A_{K_s} \sim 0.6$ mag for all the regions except for #2 and #3, where the difference is ~0.1 mag smaller and the two groups are less clearly separated.

6.1. *Dereddened* K_s *Luminosity Functions*

To assess the presence of different stellar populations between both extinction groups, we dereddened the RC features for each of them. We chose the stars belonging to each extinction group by applying the selection boxes adopted in Section 3.1 for all the regions. We decided to deredden the photometry on a star-by-star basis, applying Equation (1) to each of the target stars, as explained in Nogueras-Lara et al. (2021c). This method allowed us to have an extinction value for each of the stars in the selection boxes, avoiding the regions without any extinction value appearing in the extinction maps (which would considerably reduce the number of dereddened stars for some of the regions, biasing the results).

We produced KLFs for each region using the dereddened K_s values. Figure 10 shows the obtained results. For each luminosity function, we computed the bin width using the "auto" option implemented in the python function numpy.histogram (Harris et al. 2020). It calculates the maximum of the Freedman–Diaconis (Freedman & Diaconis 1981) and Sturges (Sturges 1926) estimators. We observed two main features whose magnitude difference and relative number of stars are significantly different between the KLFs corresponding to each of the different extinction groups, for all the regions. This confirms that there are different stellar populations associated with each of the extinction groups. Nevertheless, the KLFs corresponding to the high-extinguished stellar population appeared to present two peaks instead of the three ones detected in Section 3.1. This effect can be partially due to a smoothing of the data associated with the dereddening process (e.g., Nogueras-Lara et al. 2020a). Moreover, there is a systematic effect introduced by the bin-width selection, which has an average size of ~0.1 mag. Therefore, it is not possible to observe a difference of less than 0.2 mag. To check this, we selected different smaller bin widths and analyzed the KLF region corresponding to the main peak found for the high-extinguished stellar population. The zoom-in panels in Figure 10 show the result for three regions as an example, where the expected two-peak structure is clearly visible, in agreement with the result obtained in Section 3.1. Therefore, this analysis is consistent with the detection of different stellar populations belonging to the NSD and the NSC, respectively.

6.2. *Distance to the Features*

We computed the distance to each of the stellar populations using the mean value of the dereddened RC features for each region. For this, we fitted a Gaussian to the brightest RC peak detected for each KLF. For the high-extinguished stellar population, the Gaussian fit includes the first and the second peaks detected in Section 3.1, due to the bin-width size, as was previously explained. We did not consider the faintest peak for this population given that it does not correspond to the RC, but to the RGBB. Regarding the second peak from the low-extinguished stellar population, we did not use it given that it appears to be associated with the ~1 Gyr star formation event in the NSD (Nogueras-Lara et al. 2020b), and the RC brightness varies significantly (~0.5 mag) at this age (e.g., Girardi 2016; Nogueras-Lara et al. 2020b), hampering the use of the distance modulus to estimate the distances.

We computed the distance to each of the fitted features via the distance modulus. We assumed an absolute magnitude for RC stars of $M_{K_s} = -1.59 \pm 0.04$, as done in Nogueras-Lara et al. (2021c), averaging over the values obtained by Groenewegen (2008), Hawkins et al. (2017), and Chan & Bovy (2020). We also applied a population correction factor of $\Delta M_K = -0.07 \pm 0.07$, as explained in Schödel et al. (2010). Table 1 shows the obtained results. The uncertainties are systematic, with the statistical ones being negligible. We estimated the systematic uncertainty quadratically propagating the uncertainties involved in Equation (1). We also tested that a more in-depth analysis considering the exponential background associated with the KLF (e.g., Wegg & Gerhard 2013; Nogueras-Lara et al. 2018b) does not influence our results in any significant way within the uncertainties. We concluded that within the uncertainties, the computed distances are consistent with the measured distance to the GC of ~8 kpc. Therefore, this analysis agrees well with having stellar populations from the NSD and the NSC. We also observed that the distance toward the low-extinguished group appears to be somewhat smaller than for the high-extinguished one. Averaging over the distances obtained for each of the groups, we obtained $d_1 = 8.16 \pm 0.14$ kpc and

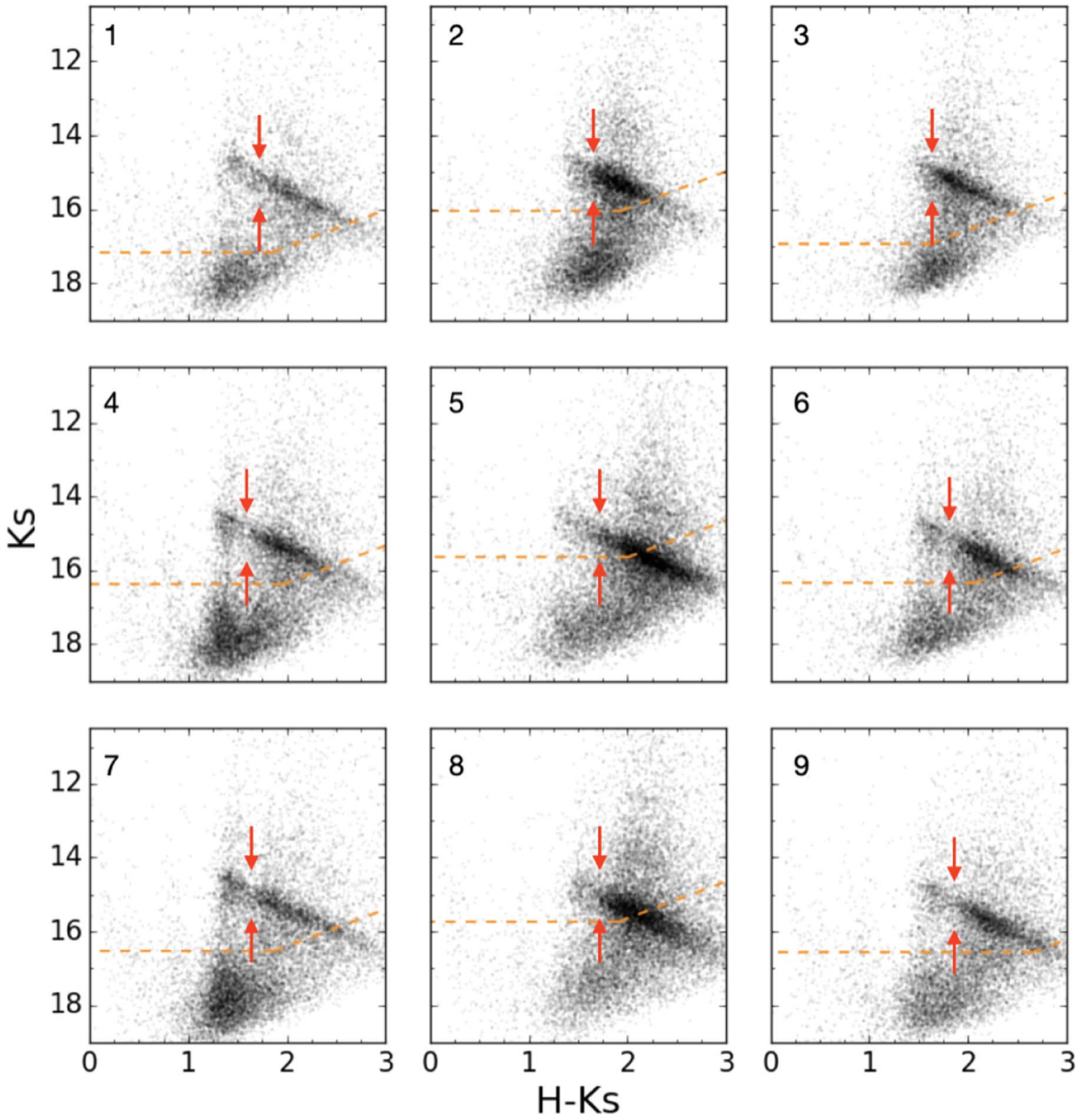

Figure 9. CMDs corresponding to different lines of sight across the observed field. The numbers in black show the associated region with respect to Figure 1. The red arrows indicate the cut between the different stellar populations observed. The stellar population corresponding to the NSD is more clearly separated for larger differences in extinction between the stellar groups (in particular it is clearly visible in panels #4 and #5). The orange dashed line represents the two-thirds completeness level.

$d_2 = 8.52 \pm 0.15$ kpc for the low- and the high-extinguished one, respectively, where the uncertainties were estimated using the standard deviation of the distribution. This is consistent with the observation of the closer edge of the NSD, given its expected radius of ∼200 pc (e.g., Launhardt et al. 2002; Nishiyama et al. 2013; Gallego-Cano et al. 2020). Moreover, this is also compatible with the lower extinction measured for the NSD, given that it would correspond to a slightly closer component in comparison with the NSC.

7. Conclusions

In this paper, we analyzed the H and K_s photometry from a region of $8\farcm2 \times 2\farcm8$ centered on the NSC. We built a K_s versus $H - K_s$ CMD and detected the presence of two different stellar groups in the RC associated with different extinctions. The different RC features detected for each of the extinction groups, and the magnitude distance between them, agree well with the stellar populations and SFHs expected for the NSD and the NSC (Nogueras-Lara et al. 2020b; Schödel et al. 2020). We checked this hypothesis using a control field in the NSD and a synthetic CMD reproducing the stellar populations from the NSD and the NSC. Using simulations, we concluded that the different RC features can be explained considering an intermediate-age stellar population in the NSC that is not present in the NSD (Schödel et al. 2020). Analogously, the faint RC feature measured for the NSD does not have a counterpart in the NSC and corresponds to a star formation event around 1 Gyr ago (e.g., Rui et al. 2019; Nogueras-Lara et al. 2020b, 2021c).

The presence of these different stellar groups with different extinctions was previously reported by Nogueras-Lara et al. (2018a), where the low-extinction group was tentatively explained

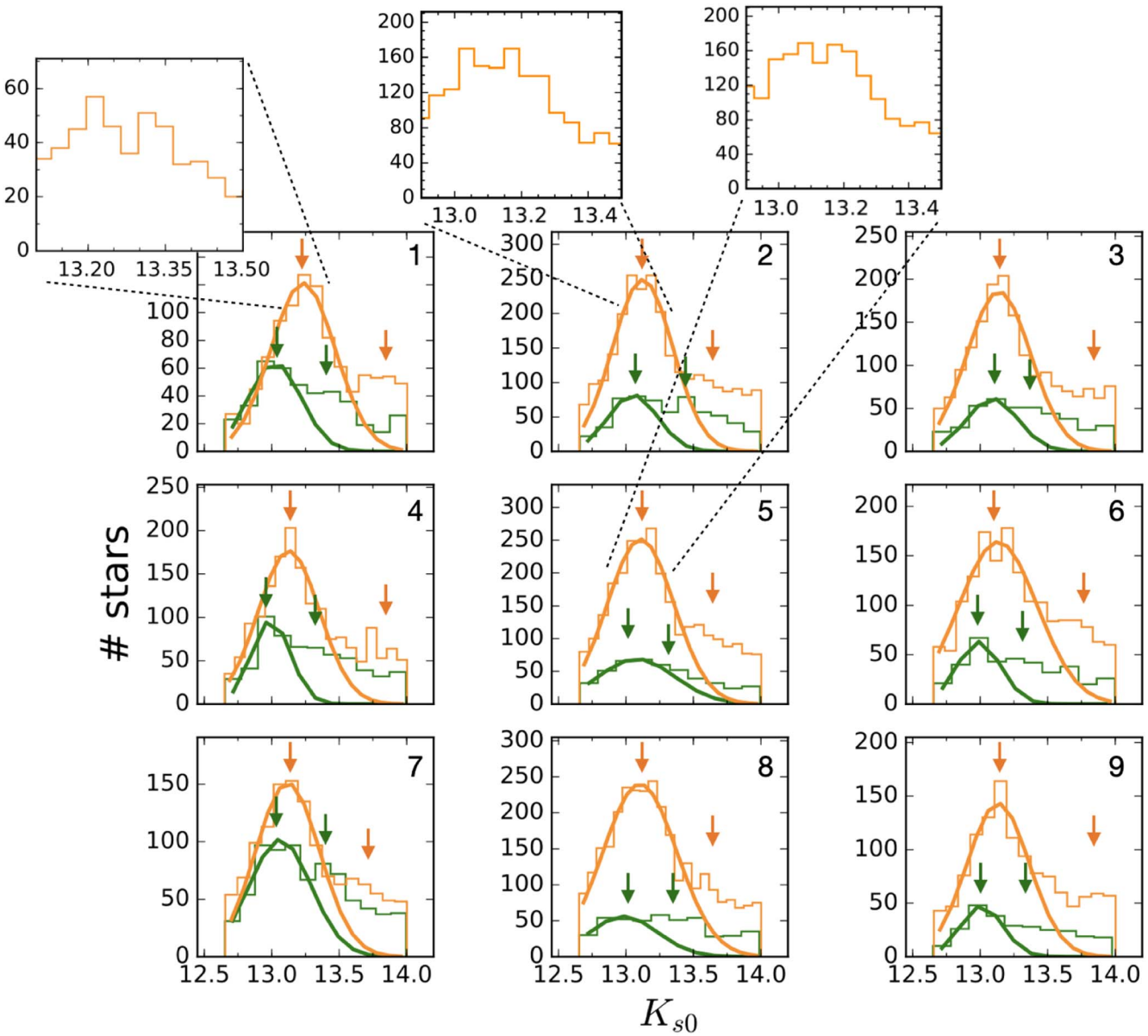

Figure 10. K_s luminosity functions observed for each of the regions in Figure 9. The green and orange histograms correspond to the low- and high-extinguished stellar groups, respectively, following the selection criteria in Section 3.1. The green and orange solid lines indicate a Gaussian fit to the brighter peak of the corresponding histogram. The green and orange arrows mark the features observed in the KLFs. The zoom-in panels show how the bright peak of the high-extinguished stellar population corresponds to two close peaks.

Table 1
Average Dereddened RC Magnitudes and Distances

Region	$K_{s0\ 1}$ (mag)	$K_{s0\ 2}$ (mag)	d_1 (kpc)	d_2 (kpc)
1	13.02	13.23	8.1 ± 0.5	8.9 ± 0.5
2	13.05	13.12	8.2 ± 0.5	8.5 ± 0.5
3	13.09	13.14	8.4 ± 0.5	8.5 ± 0.5
4	13.00	13.13	8.0 ± 0.4	8.5 ± 0.5
5	13.08	13.11	8.3 ± 0.5	8.4 ± 0.5
6	12.99	13.13	8.0 ± 0.4	8.5 ± 0.5
7	13.06	13.12	8.3 ± 0.5	8.5 ± 0.5
8	12.98	13.10	8.0 ± 0.4	8.4 ± 0.5
9	13.01	13.13	8.1 ± 0.4	8.5 ± 0.5

Note. $K_{s0\ 1}$ and $K_{s0\ 2}$ indicate the dereddened K_s magnitudes corresponding to the main peaks in the KLFs for the low- and the high-extinguished stellar groups, respectively. The associated uncertainties are $\Delta K_s \sim 0.12$ mag and correspond to systematics, with the statistical uncertainty negligible. d_1 and d_2 correspond to the associated distance of each of the stellar groups. For relative comparison between the distances corresponding to the different features, the uncertainty is ~20% lower.

as a stellar feature in front of the central molecular zone (e.g., Morris & Serabyn 1996). According to our results, we believe that this scenario is improbable. Building extinction maps, we conclude that the low-extinguished stellar population belongs to the NSD.

Finally, we computed the distance toward the NSD and the NSC, creating dereddened KLFs and fitting them with a Gaussian model. The results agree with the expected GC distance. Moreover, we found some evidence of a slightly closer distance to the stellar population from the NSD, which appears to be 360 ± 200 pc closer to us. This is in agreement with the observation of the stars from the closest edge of the NSD, considering its radius of $\sim$200 pc.

Our results show that the NSD and the NSC are detectable due to significantly different extinctions along the line of sight toward the NSC and point toward the presence of different stellar populations associated with a different SFH and formation scenario of both components.

This work is based on observations made with ESO Telescopes at the La Silla Paranal Observatory under programme IDs 195.B-0283 and 091.B-0418. We thank the staff of ESO for their great effort and helpfulness. F.N.-L. acknowledges the sponsorship provided by the Federal Ministry for Education and Research of Germany through the Alexander von Humboldt Foundation. F.N.-L. and N.N. gratefully acknowledge support by the Deutsche Forschungsgemeinschaft (DFG, German Research Foundation) Project-ID 138713538 SFB 881 ("The Milky Way System", subproject B8). R.S. acknowledges financial support from the State Agency for Research of the Spanish MCIU through the "Center of Excellence Severo Ochoa" award for the Instituto de Astrofísica de Andalucía (SEV-2017-0709). R.S. acknowledges financial support from national project PGC2018-095049-B-C21 (MCIU/AEI/FEDER, UE).

ORCID iDs

Francisco Nogueras-Lara https://orcid.org/0000-0002-6379-7593
Rainer Schödel https://orcid.org/0000-0001-5404-797X
Nadine Neumayer https://orcid.org/0000-0002-6922-2598

References

Akaike, H. 1974, ITAC, 19, 716
Bressan, A., Marigo, P., Girardi, L., et al. 2012, MNRAS, 427, 127
Chan, V. C., & Bovy, J. 2020, MNRAS, 493, 4367
Chen, Y., Bressan, A., Girardi, L., et al. 2015, MNRAS, 452, 1068
Chen, Y., Girardi, L., Bressan, A., et al. 2014, MNRAS, 444, 2525
Diolaiti, E., Bendinelli, O., Bonaccini, D., et al. 2000, Proc. SPIE, 4007, 879
Do, T., Hees, A., Ghez, A., et al. 2019, Sci, 365, 664
Eisenhauer, F., Quirrenbach, A., Zinnecker, H., & Genzel, R. 1998, ApJ, 498, 278
Feldmeier-Krause, A., Kerzendorf, W., Neumayer, N., et al. 2017, MNRAS, 464, 194
Ferraro, F. R., Dalessandro, E., Mucciarelli, A., et al. 2009, Natur, 462, 483
Freedman, D., & Diaconis, P. 1981, Z. Wahrscheinlichkeitstheorie verw Gebiete, 57, 453
Gallego-Cano, E., Schödel, R., Nogueras-Lara, F., et al. 2020, A&A, 634, A71
Genzel, R., Eisenhauer, F., & Gillessen, S. 2010, RvMP, 82, 3121
Girardi, L. 2016, ARA&A, 54, 95
Graham, A. W., & Spitler, L. R. 2009, MNRAS, 397, 1003
Gravity Collaboration, Abuter, R., Amorim, A., et al. 2018, A&A, 615, L15
Groenewegen, M. A. T. 2008, A&A, 488, 935
Harris, C. R., Millman, K. J., van der Walt, S. J., et al. 2020, Natur, 585, 357
Hawkins, K., Leistedt, B., Bovy, J., & Hogg, D. W. 2017, MNRAS, 471, 722
Kissler-Patig, M., Pirard, J.-F., Casali, M., et al. 2008, A&A, 491, 941
Launhardt, R., Zylka, R., & Mezger, P. G. 2002, A&A, 384, 112
Marigo, P., Girardi, L., Bressan, A., et al. 2017, ApJ, 835, 77
Morris, M., & Serabyn, E. 1996, ARA&A, 34, 645
Nagayama, E., Nagashima, O., Nakajima, D., et al. 2003, Proc. SPIE, 4841, 459
Nataf, D. M., Udalski, A., Gould, A., & Pinsonneault, M. H. 2011, ApJ, 730, 118
Nishiyama, S., Nagata, T., Kusakabe, N., et al. 2006, ApJ, 638, 839
Nishiyama, S., Nagata, T., Tamura, M., et al. 2008, ApJ, 680, 1174
Nishiyama, S., Yasui, K., Nagata, T., et al. 2013, ApJL, 769, L28
Nogueras-Lara, F., Gallego-Calvente, A. T., Dong, H., et al. 2018a, A&A, 610, A83
Nogueras-Lara, F., Schödel, R., Dong, H., et al. 2018b, A&A, 620, A83
Nogueras-Lara, F., Schödel, R., Gallego-Calvente, A. T., et al. 2019b, A&A, 631, A20
Nogueras-Lara, F., Schödel, R., Gallego-Calvente, A. T., et al. 2020b, NatAs, 4, 377
Nogueras-Lara, F., Schödel, R., Najarro, F., et al. 2019a, A&A, 630, L3
Nogueras-Lara, F., Schödel, R., Neumayer, N., et al. 2020a, A&A, 641, A141
Nogueras-Lara, F., Schödel, R., & Neumayer, N. 2021a, A&A, 653, A33
Nogueras-Lara, F., Schödel, R., & Neumayer, N. 2021b, A&A, 653, A133
Nogueras-Lara, F., Schödel, R., Neumayer, N., & Schultheis, M. 2021c, A&A, 647, L6
Pastorelli, G., Marigo, P., Girardi, L., et al. 2019, MNRAS, 485, 5666
Pastorelli, G., Marigo, P., Girardi, L., et al. 2020, MNRAS, 498, 3283
Pedregosa, F., Varoquaux, G., Gramfort, A., et al. 2011, JMLR, 12, 2825
Rui, N. Z., Hosek, M. W., Lu, J., et al. 2019, ApJ, 877, 37
Schödel, R. 2011, in ASP Conf. Ser., 439, ed. M. R. Series, Q. D. Morris, & F. Wang (San Francisco, CA: ASP), 222
Schödel, R., Feldmeier, A., Neumayer, N., Meyer, L., & Yelda, S. 2014, CQGra, 31, 244007
Schödel, R., Najarro, F., Muzic, K., & Eckart, A. 2010, A&A, 511, A18
Schödel, R., Nogueras-Lara, F., Gallego-Cano, E., et al. 2020, A&A, 641, A102
Schödel, R., Yelda, S., Ghez, A., et al. 2013, MNRAS, 429, 1367
Schultheis, M., Fritz, T. K., Nandakumar, G., et al. 2021, A&A, 650, A191
Schultheis, M., Rich, R. M., Origlia, L., et al. 2019, A&A, 627, A152
Schwarz, G. 1978, AnSta, 6, 461
Sormani, M. C., Magorrian, J., Nogueras-Lara, F., et al. 2020, MNRAS, 499, 7
Sturges, H. A. 1926, J. Am. Stat. Assoc., 21, 65
Tang, J., Bressan, A., Rosenfield, P., et al. 2014, MNRAS, 445, 4287
Wegg, C., & Gerhard, O. 2013, MNRAS, 435, 1874